Photonic-chip based free space beam shaping and steering for advanced optical microscopy application

MARCEL LAHRBERG, FIREHUN TSIGE DULLO, AND BALPREET SINGH AHLUWALIA* iD

Department of Physics and Technology, UiT The Arctic University of Norway, NO-9037 Tromsø, Norway
*balpreet.singh.ahluwalia@uit.no

Abstract: Photonic-chip-based light illumination has recently found applications in optical microscopy and nanoscopy methodologies. The photonic chip removes the dependency on imaging objective lenses to generate the required illumination patterns for different microscopy methods. Until now, all the reported chip-based optical microscopy methods exploit the evanescent field present on top of a waveguide surface and are thus inherently limited to two-dimensional microscopy. Here, we perform systematic simulation studies to investigate different chip-based waveguide designs for static and dynamic shaping of light beams in the free-space. The simulation studies have been carefully designed considering the photo-lithography limitations and wavelength spectrum (405 nm to 660 nm) that is of interest in fluorescence based optical microscopy and nanoscopy. We first report the generation of a quasi-Bessel beam (QBB) using an on-chip axicon made at the end facet of a planar waveguide to mimic light sheet illumination. This is extended to the implementation of a counter propagating QBB for lattice light-sheet applications. The double axicon, a derivative of the axicon generates superimposed Bessel beams (SBB). Its waveguide-based implementation is proposed and analyzed. Finally, we investigate an optical phased array (OPA) approach to allow dynamic steering of the output light in the free-space. The aim of this study is to find suitable waveguide design parameters for free-space beam shaping operating in the visible spectrum opening possibilities for three-dimensional chip-based optical microscopy.

1.   Introduction

The last decade has witnessed momentous progress in the field of advanced optical microscopy with focus on two fronts. These are super-resolution (SR) optical microscopy commonly referred to as optical nanoscopy that has overcome what is generally known as the Abbe diffraction limit in the field of optical microscopy, and minimally invasive, three-dimensional light sheet fluorescence microscopy (LSFM) or selective plane illumination microscopy (SPIM). Optical nanoscopy comprises a panel of techniques including structured illumination microscopy (SIM) [1,2], stimulated emission depletion (STED) [3] microscopy, and single-molecule localization microscopy (SMLM) techniques such as photo activated localization microscopy (PALM) [4] and fluorescence photoactivation localization microscopy (FPALM) [5] as well as stochastic optical reconstruction microscopy (STORM) [6] and direct STORM (dSTORM) [7]. Techniques such as SR optical fluctuation imaging (SOFI) [8] and entropy-based SR imaging (ESI) [9] are based on the analysis of signal fluctuations in an acquired image series. LSFM or SPIM [10], originally developed as orthogonal-plane fluorescence optical sectioning (OPFOS) [11], uses orthogonal illumination of the sample with respect to the imaging objective lens, minimizing out-of-focus light and providing exceptional optical sectioning capability. This has made LSFM a most suitable method for live cell imaging of thick specimens.

Most of the present day advanced optical microscopy uses complex and costly optical microscopes to deliver specialized illumination patterns required to achieve high-resolution images while the sample lies on a simple glass slide. These advanced microscopy solutions all employ bulk optics for laser beam engineering in free-space and a microscope to deliver the illumination pattern. This approach is prone to misalignment; therefore, successful implementation requires well-calibrated optics hosted on a stable and mechanically rigid platform, consequently increasing their cost and hindering parallelization.

Recently, photonic-chip-based optical fluorescence nanoscopy has emerged as a potential solution to reduce the system complexity and cost of present day optical nanoscopy [12–16]. The light inside the waveguide is guided based on total internal reflection (TIR), generating an evanescent field at the core and cladding interface. In chip-based optical nanoscopy the sample is placed directly on top of an optical waveguide (the core) and is illuminated using the evanescent field present at the interface. The fluorescence signal is collected using any standard upright optical microscope. Waveguide chip illumination generates evanescent field excitation, which is determined by the waveguide geometry (length and width) and is independent of the imaging objective lens. The illumination and collection light paths are therefore decoupled in photonic-chip-based microscopy. These properties of on-chip illumination have recently been exploited in chip-based dSTORM and ESI [17,18] and SIM [19]. Chip-based optical nanoscopy does not only hold edge over conventional approaches on simplicity and cost but has also pushed the technical frontiers of respective optical nanoscopy methodologies. On-chip dSTORM has demonstrated the largest field of view (FoV) ever reported with super-resolution (70 nm resolution over 500 μm × 500 μm), 100-times larger than the conventional solution. Similarly, on-chip SIM was demonstrated with 2.4-fold resolution enhancement with respect to conventional microscopy, contrary to a 2-fold improvement of conventional SIM.

However, all on-chip optical microscopy and nanoscopy approaches so far have been limited to two-dimensional imaging, as they use the evanescent field present on top of the waveguide surface. Thus only a thin portion of the cell (e.g. 150 nm to 200 nm) touching the waveguide surface can be imaged due to evanescent field excitation. For three dimensional and volumetric imaging of the sample it is necessary to access the light guided inside the waveguide and to perform beam shaping in the free-space. To access the guided light inside the waveguide, there could be different approaches to do so. The end of the waveguide can be cleaved [20,21] and the light escaping from the end facet can be used for 3D imaging. Alternatively, it is also possible to use a grating coupler to out-couple the guided light inside the waveguide [22]. Most of the grating couplers are optimized for a single wavelength and have less tolerance for a wide span of wavelengths that are intended to be used in fluorescence based optical microscopy, spanning from 405 nm to 660 nm, which is focus of this work. Therefore, in this study the outcoupling is performed by means of cleaved end facets as it would be less prone to errors over a wide wavelength spectrum.

Previous developments related to on-chip beam shaping are silicon on insulator (SOI) based implementations that are inherently restricted to work using infrared wavelengths, opposed to the visible wavelength spectrum (405 nm to 660 nm) that is of interest for optical microscopy. They comprise light detection and ranging (Lidar) [23], near-field-focusing [24], QBB generation [25,26] and beam steering [22,27]. Silicon nitride (Si_3N_4) based OPAs have been demonstrated to work at a visible vacuum wavelength of 635 nm [28].

In this work, we investigate on-chip light shaping strategies for the visible wavelength spectrum (405 nm to 660 nm) with the aim to be used in optical microscopy and optical nanoscopy applications. While on-chip axicon like designs have been previously explored, here we extend the scope for photonic-chip-platforms for the generation of self-imaged optical beams and lattice-like light sheets for the first time to the best of our knowledge. Moreover, we extend the

use of integrated optical arrays to generate user-defined self-imaged optical beams and Bessel beams at visible wavelength and investigate their usefulness from optical microscopy application.

The light from the cleaved end of the waveguide would diverge rapidly, therefore on-chip lenses at the end facets of the waveguide were simulated and investigated. Here, first we discuss the design and simulation of on-chip integrated lenses (axicons) that are necessary to generate single plane static illumination using a photonic chip in section 2. Such a single plane light illumination will find application in light sheet microscopy. In order to generate steerable light illumination, an integrated OPA approach is explored in section 3. The simulation parameters investigated in this study carefully consider both the fabrication tolerance of the conventional photolightography that governs the waveguide designs, and the practical requirements of the desired illumination pattern, such as dimensions, divergence, wavelength and beam shaping that are essential in optical microscopy for bioimaging applications.

2. Design and simulation of chip-based static beam shaping in free space

The diffraction of light is inextricably connected to its wavelike nature; it is governed by the Helmholtz equation [29]. This means that propagating light shows divergence in most cases, especially after hitting an object along the direction of propagation. However the Bessel beam is a nondivergent solution of the Helmholtz equation [30,31]. It has a lateral intensity profile that is described by a Bessel function and does not change along the direction of propagation. In addition the Bessel beam also shows self-reconstruction, sometimes called self-healing, after hitting an obstacle along the way of propagation [32]. The electric field amplitude of the zeroth-order Bessel beam can be written as [30]

$$E_j(\rho, x) = J_0(k_{\rho j}\rho) \exp\left[i\left(k_{xj}x + \phi_j\right)\right], \tag{1}$$

where ρ is the transverse distance from the optical axis, x is the direction of propagation along the optical axis, $k_j = \frac{2\pi}{\lambda_j}$ is the wave vector with wavelength λ_j and its radial and longitudinal components $k_{\rho j}$ and k_{xj}, the index j refers to a particular Bessel beam. The term J_0 is the zeroth-order Bessel function of first kind. The intensity of the Bessel beam is proportional to

$$I_j(\rho) \propto J_0^2\left(k_{\rho j}\rho\right) \tag{2}$$

and is independent of x; which highlights the non-diverging property of ideal Bessel beam. This holds for beams of infinite lateral extend resulting in an infinite amount of energy in the beam since J_0 is not square-integrable [30]. It is possible though to experimentally realize a QBB that shows the described properties over a finite propagation length without the necessity of infinite lateral extend.

It has been shown that the interference of two Bessel beams ($j = 1$ and $j = 2$), with different radial propagation constants generates an interference pattern of the electric field amplitudes $E_1(\rho, x)$ and $E_2(\rho, x)$ propagating on a common optical axis; the SBB whose intensity distribution is proportional to [33]

$$I(\rho, x) \propto J_0^2\left(k_{\rho 1}\rho\right) + J_0^2\left(k_{\rho 2}\rho\right) + 2J_0\left(k_{\rho 1}\rho\right) J_0\left(k_{\rho 2}\rho\right) \times \cos\left[(k_{x1} - k_{x2})x + \phi_1 - \phi_2\right]. \tag{3}$$

This interference pattern shows zero intensity spots on the optical axis that are surrounded by non-zero light intensity, it may be referred to as a bottle beam. The bottling is governed by the cos-term in Eq. (3) for $k_{x1} - k_{x2} \neq 0$.

Experimentally a Bessel beam can be generated by passing collimated light through an axicon, for example an annular slit in the focal plane of a lens, generating an interference pattern [34] where the author refers to van Heel [35] who used such a geometry for two-dimensional alignment problems. Although any rotationally symmetric optical element that images a point source into a

stretch along the optical axis [36] may be referred to as an axicon, the most common type is a glass cone and the Bessel beam is generated by passing a Gaussian beam through it [37].

It is noted that the described generation of a fundamental QBB is based on feeding a fundamental Gaussian beam (fundamental Laguerre-Gaussian mode) into the axicon. It is possible to generate higher order Bessel beams by passing Laguerre-Gaussian laser modes with a radial or azimuthal index not equal to zero through an axicon. These higher order Bessel beams exhibit a modified beam structure that has also been used to generate bottle beams [38,39].

2.1. Choice of waveguide material

The careful choice of suitable material is an important first step. In section 2, the waveguide designs are simulated using Si_3N_4 and in section 3 it is based on tantalum pentoxide (Ta_2O_5). High-refractive index material such as Si_3N_4 and Ta_2O_5 enable ultra-compact waveguide structures with small bend radii and thus compact footprint on an integrated optical functions. In particular Si_3N_4 has gained significant popularity in recent years, due to it is compatibility with conventional semiconductor fabrication facilities, high-refractive index ($n = 2.0$ @ 532 nm) and low loss.

2.2. On-chip axicon design

The light pattern generation presented in the following is based on planar waveguide technology as illustrated in Fig. 1. Light coupled into the input facet of the waveguide chip can propagate in well defined modes in the waveguide. Single mode waveguide condition is necessary to control the beam shaping in the free-space. In previous work, single mode conditions at visible wavelengths (405 nm to 660 nm) were achieved using shallow rib geometry [12]. The advantage of rib waveguide geometry over strip waveguide is that it allows single mode behaviour for wider waveguide geometry [12].
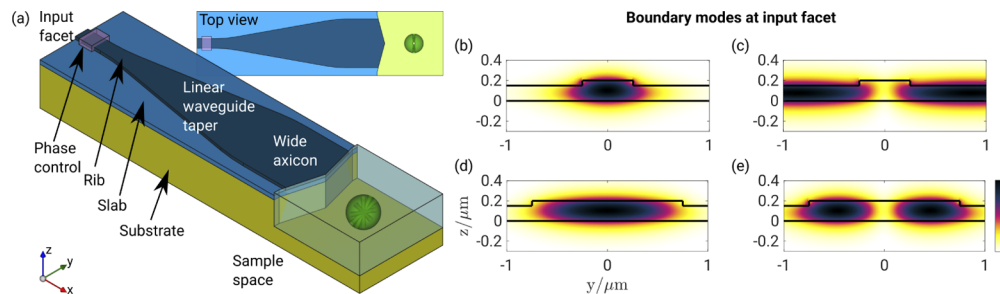

Fig. 1. A rib waveguide using a linear waveguide taper in order to maintain the fundamental mode. Panel **(a)** shows the general rib waveguide under consideration. Boundary modes **(b)**-**(e)** for a model at a vacuum wavelength of 660 nm with materials of refractive indices 1.46 (Substrate, SiO_2), 2.12 (Slab and Rib, Ta_2O_5), and 1.33 (water on top). The slab and rib height are set to 200 nm and 50 nm respectively. In **(b)** the fundamental waveguide mode for a rib waveguide of 500 nm width is shown. It is the only guided mode, the first order mode **(b)** (mode with next lower effective refractive index) is not guided (propagates in the slab). For a rib waveguide with a rib width of 1.5 µm not only the fundamental mode **(d)**, but also the first order mode **(e)** is guided in the waveguide. The boundary modes are presented as the norm of their electric field distribution in arbitrary units, color bar in **(d)**.

Given a small enough rib width (here 500 nm) only the fundamental mode **(b)** is guided. The next waveguide mode (with the next lower effective index) is not guided, it is a slab mode as shown in **(c)**, i.e. propagating outside the waveguide core. However, for bio-imaging the main interest is on wider waveguides to generate a large beam to scan the entire cells (10 µm to 20 µm).

A wide waveguide made of Si_3N_4 will not only guide the fundamental mode **(d)** but also the higher order modes, for example the first order mode as shown in **(e)**. To solve this issue, a single mode waveguide is used at the input facet and is adiabatically tapered out as illustrated in **(a)**. Light is coupled into the waveguide, only exciting the fundamental mode of the narrow input. The adiabatic waveguide taper expands the mode into the fundamental mode of the wider waveguide part without exciting higher order modes. This way a pure single mode condition can be maintained using a Si_3N_4 rib waveguide. In addition a phase shift of the guided mode can be achieved by means of thermo-optic manipulation as indicated in **(a)**.

In the first approximation, generating a 1D-QBB by means of an axicon can be described in terms of a combination of geometrical optics and wave optics as presented in Fig. 2. Figure 2**(a)** shows a general design of a chip-based axicon, with the axicon structure in the *xy*-plane like a cross section of a conventional rotationally symmetric axicon. The waveguide core, i.e. the slab and the rib is made of Si_3N_4 on a SiO_2 substrate. The light inside the waveguide is tightly confined in both axes, thus it will diverge rapidly from the end facet of the waveguide. For hosting the sample and for the generation of the beam, it will be essential to etch away both the core (rib and slab) and the underlying cladding at the end facet. The axicon at the end facet is used to control the divergence of the beam in the *xy*-plane, generating a line focus as shown in Fig. 2**(b)**. The top view in Fig. 2**(b)** indicates the QBB properties of the propagating light in the *xy*-plane. However, the divergence in the *xy*-plane is allowed intentionally as shown by the red region of Fig. 2**(a)**. The net result is a thin light sheet illumination. Using Fig. 2**(c)**, showing one half of the cross section and Fig. 2**(d)**, showing a full cross section, the propagation of the light is described in terms of geometrical optics and the wave properties are only taken into account to describe the generated interference pattern. Collimated light propagating along the optical axis enters the axicon from the left-hand side. Assuming that the whole axicon aperture of size $2R$ is filled (R being the half width of the waveguide), the light is refracted by the conical surface (characteristic wedge angle α) and propagates over the red shaded area. The refractive index of the axicon is n_i and the refractive index of the environment n_o, where $n_i > n_o$. Using Snell's law, the light coming from the upper part of the axicon is incident onto the optical axis at an angle $\theta = \arcsin\left(\sin(\alpha)\frac{n_i}{n_o}\right) - \alpha$. The length along the optical axis over which light coming from the axicon is incident on the optical axis and thus generating the Bessel beam is given by the DOF (see Fig. 2**(c)** and **(d)**)

$$\text{DOF} = x^{\max} - x^{\min}, \tag{4}$$

with $x^{\min} = R\tan(\alpha)$ and $x^{\max} = \frac{R}{\tan(\theta)}$. The maximum width over which the interference takes place is given by $W = \text{DOF}\tan(\theta)$ and the fringe spacing of the resulting interference pattern is given by what is commonly referred to as the Abbe diffraction limit $\Delta r = \frac{\lambda_0}{2\text{NA}}$, with the vacuum wavelength λ_0 and the numerical aperture $\text{NA} = n_0\sin(\theta)$. This allows to calculate the number of intensity lobes to be

$$N_{\text{lobes}} = \frac{W}{\Delta r}. \tag{5}$$

From the physics point of view it seems reasonable to round these values to the nearest odd integer. Viewing the Bessel beam as an interference pattern of plane waves propagating at a fixed angle with the optical axis explains the self-healing properties of the beam since the Bessel beam does not consist of light propagating along the optical axis, liming the shadow of an object along the optical axis depending on its size and the angle θ. For the application in LSFM the Bessel beam should optimally provide a large DOF at a limited Δr with only one strong central lobe. This can be achieved by balancing the values of R and θ [26].

Next, the generation of one-dimensional SBB using a photonic-chip is investigated. In order to generate SBB by overlapping two zeroth order QBBs, three basic principles have been employed so far. First, a screen with two annular slits of different radii and a lens were used to generate the SBB, demonstrating the self imaging effect in a non-diffracting beam [33]. Then the self-imaged
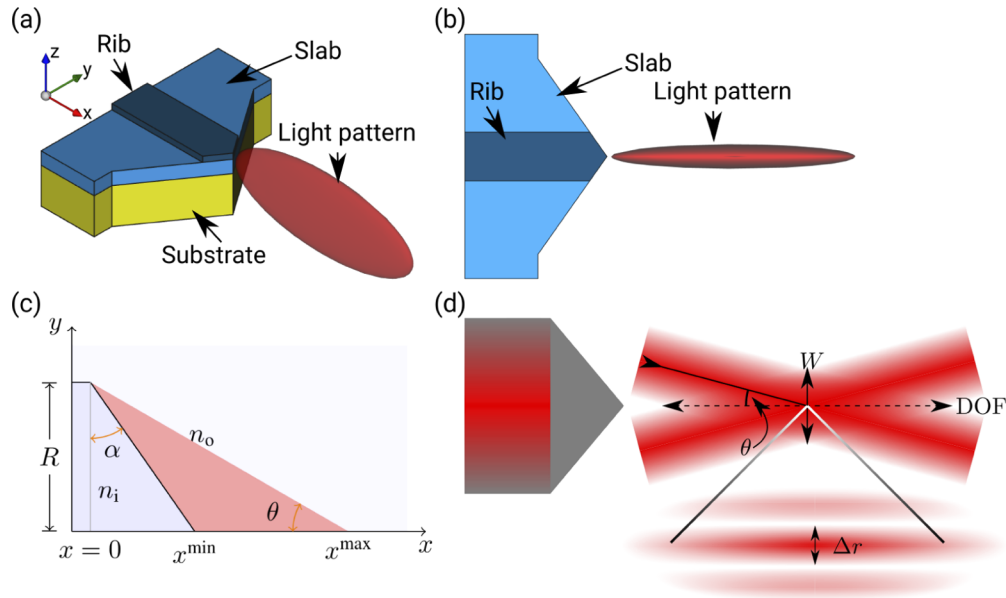
Fig. 2. The chip-based axicon and its ability to form a 1D light sheet as part of 1D-QBB. In **(a)** a general design for an axicon using a planar waveguide and the beam shaping capability is shown. The top view in **(b)** shows the *xy*-plane where the 1D-QBB intensity profile is generated. Following [26], the DOF of the generated QBB profile can be approximated using the optical properties and geometry shown in **(c)** where only one half of the top view is presented. Describing the QBB as an interference pattern can be done using the sketch in **(d)**, where the axicon is set of to the left for better visualization.

bottle beam was introduced by using a hologram on a spatial light modulator (SLM) [40] as well as a photolithography hologram [41]. On the other hand, starting with a highly efficient glass cone axicon, introducing a second wedge angle it is possible to obtain a so called double axicon. Passing a fundamental Gaussian beam through this optical device it is possible to generate two overlapping zeroth-order QBBs with different longitudinal wave vector components, interfering on the optical axis and generating the SBB [42–44].

More involved implementations using an SLM for spatial filtering have been shown to significantly improve the propagation length [45]. A slightly different way to generate self-imaging beams is a volume holographic method using a Bessel readout beam [46].

In Fig. 3 the light shaping function of the double axicon, similar to what is done in Fig. 2 with respect to the (single) axicon, is described. The refractive index of the axicon is n_i and the refractive index of the environment n_o, where $n_i > n_o$. The axicon has two angles with $\alpha_1 > \alpha_2$. The radii of the axicons are given by $R_1 > R_2$. Again, using Snell's law, the angle between the light coming from the upper part of the axicon and the optical axis is θ_1. The light coming from the lower part of the axicon forms an angle with the optical axis of θ_2. For the given conditions, the refractive indices and axicon angles it follows $\theta_1 > \theta_2$ with $\theta_{1/2} = \arcsin\left(\sin\left(\alpha_{1/2}\right) \frac{n_i}{n_o}\right) - \alpha_{1/2}$. The distance over which light coming from the outer axicon in incident on the optical axis is given by $x_1^{min} = \tan\left(\alpha_1\right)\left(R_1 - R_2\right) + \frac{R_2}{\tan(\theta_1)}$ and $x_1^{max} = \frac{R_1}{\tan(\theta_1)}$. For the light coming from the lower axicon this distance is given by $x_2^{min} = \tan\left(\alpha_1\right)\left(R_1 - R_2\right) + \tan\left(\alpha_2\right)R_2$ and $x_2^{max} = \tan\left(\alpha_1\right)\left(R_1 - R_2\right) + \frac{R_2}{\tan(\theta_2)}$.
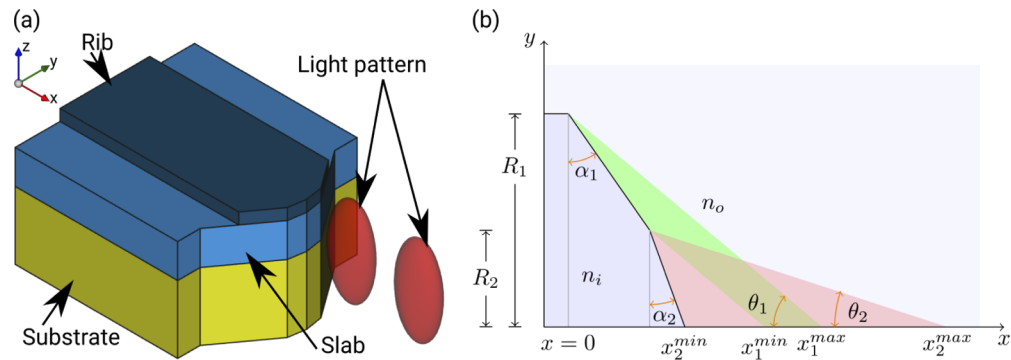
Fig. 3. The chip-based double axicon and its ability to form a light sheet as part of a SBB. In **(a)** a general design for a double axicon using a planar waveguide and the beam shaping capability is shown. In **(b)**, as for the (single) axicon in Fig. 2**(c)**, the necessary parameters to approximate the interaction length along the optical axis, where a SBB profile may be generated, is shown.

2.3. Finite element simulation

The on-chip axicon represents a cross-section of an actual axicon that is described as a rotationally symmetric device. It is the deliberate attempt to limit the non-divergent properties of the QBB to one plane and being able to manipulate the light in the direction perpendicular to that plane in a different way. The two-dimensional implementation of the axicon on a planar waveguide is proposed elsewhere [26], where finite-difference time-domain (FDTD) simulations of Si_3N_4 for vacuum wavelength in the infrared (780 nm) are shown. The idea is to perform light sheet microscopy where the light sheet is generated by a one-dimensional axicon. It is estimated that light sheets with a resolution of twice the wavelength of the used light can be generated. In the following two-dimensional simulations of the proposed (double) axicons are performed assuming a waveguide design similar to the sketches in Fig. 2**(c)** and Fig. 3**(b)** using the refractive index of Si_3N_4 and water at a given vacuum wavelength for the simulation of 532 nm.

2.3.1. Waveguide based axicons

In Fig. 4 a two-dimensional simulation for on-chip axicon as described above with $R = 20\ \mu m$ at a visible vacuum wavelength of $\lambda_0 = 532$ nm, $n_i = 2.0559$, $n_o = 1.3371$, and different angles α is presented. The simulations are done using the finite element method (FEM) in COMSOL Multiphysics (COMSOL) and the results are presented as the square of the electric field norm as a measure of the intensity distribution. As can be seen in Fig. 4**(a)** the smaller the wedge angle the larger is the non-diffracting distance of the central core of the Bessel beam. Also, Fig. 4**(a)** shows that the on-chip axicon output does not only consist of the central beam or lobe, but also some weak side lobes. Although the number of lobes according to Eq. (5) is rather high with 5, 7, 9, 11 and 15 for **(a)**–**(e)** respectively, it is observed that the further away from the central lobe these side lobes appear, the farther along the propagation direction they show maximum intensity. Even though the side lobes are not desirable for conventional light sheet microscopy, the appropriate placement of the side lobes could be exploited for simultaneous imaging of multiple planes.

This is the reason why the investigation of the proposed waveguide designs, using geometrical optics only is not sufficient anymore and the wavelike nature of light has to be considered more rigorous. The number of lobes to be expected according to Eq. (5) would render the investigated axicons with the parameters given in Fig. 4 useless with respect to an application in light sheet generation, as it has been pointed out already [26]. As can be seen in Fig. 4 the central maximum is rather limited to extend in the first half of the DOF, whereas the side lobes are more prominent
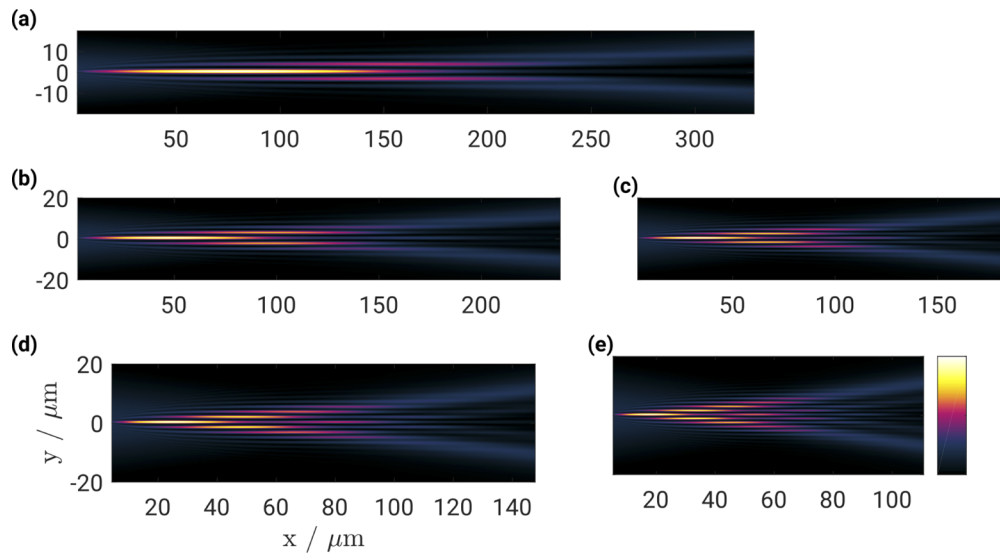
Fig. 4. Simulation results for an axicon with $R = 20\,\mu m$ at a vacuum wavelength of $\lambda_0 = 532$ nm, $n_i = 2.0559$, $n_o = 1.3371$. Shown are the values for the electric field norm squared in arbitrary units for **(a)** $\alpha = 6°$, **(b)** $\alpha = 8°$, **(c)** $\alpha = 10°$, **(d)** $\alpha = 12°$, and **(e)** $\alpha = 15°$.

in the region farther away for the the axicon. This is also visible in Fig. 5**(a)** where the intensity profile for the central maximum along the direction of propagation extracted from the results presented in Fig. 4 is shown. Increasing the axicon angle does not only shorten the relevant propagation of the central lobe and increase the number of side lobes, but it also introduces intensity variations along the direction of propagation. In order to assess the validity of the geometrical description, the FWHM of the central beam at its maximum (along x) is compared to the FWHM as predicted by $\frac{\Delta r}{2}$ in Fig. 5**(b)**. It suggests that the geometrical optics based approach is an overall valid approximation although the physically more precise FEM simulations predict a slightly larger FWHM for the central maximum. The intensity fluctuations along the optical axis as seen in Fig. 5**(a)** emphasize the necessity of FEM simulations since these fluctuations cannot be predicted using the geometrical optics based model. Finally it can be observed that the translation invariant property of the field amplitude reduces over a finite length.

2.3.2. Size variation in on-chip axicons

Increasing the size of the axicon from $R = 20\,\mu m$ to $R = 40\,\mu m$ changes the interference pattern generated by the axicon as shown in Fig. 6. First of all it can be seen that the number of lobes increases. The geometrical approximation predicts 7 and 15 lobes for an axicon angle of 8°. As for the axicon with $R = 20\,\mu m$, the side lobes appear farther along the direction of propagation especially those that are generated more distant from the optical axis. According to Eq. (4) an increase in R also increases the propagation length of the central maximum. Looking at Fig. 6**(b)** and **(c)** it can be seen that the intensity along the optical axis does not stay constant but is rather extended in a modulated fashion. This puts a much shorter limit to the application of on-chip axicon for the generation of light sheets for imaging application. For bio-imaging it is desirable that different parts of the sample is illuminated with similar intensities.

Moreover, it can be seen that the relevant propagation distance for the central beam is much shorter than the DOF predicted by the geometry which would be $260\,\mu m$ for $R = 20\,\mu m$ and $520\,\mu m$ for $R = 40\,\mu m$. In addition to that is the number of lobes with 7 and 15 for $R = 20\,\mu m$ and $R = 40\,\mu m$ respectively much larger than the number of lobes appearing over the first $100\,\mu m$

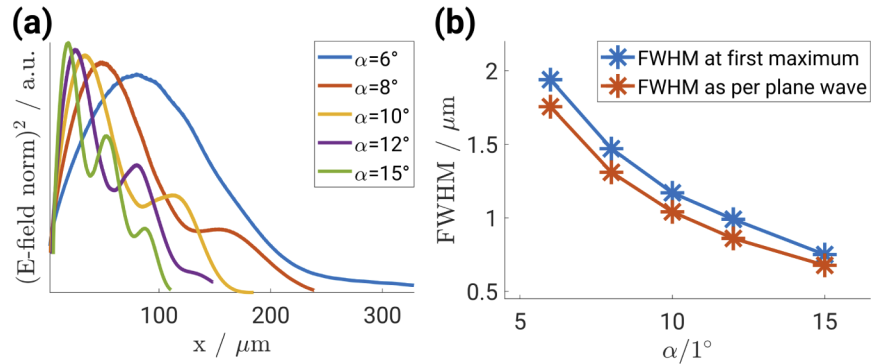**Fig. 5.** The central beam along the optical axis as simulated for an axicon with $R = 20$ μm at a vacuum wavelength of $\lambda_0 = 532$ nm, $n_i = 2.0559$, $n_o = 1.3371$ and varying axicon angles α using FEM is evaluated. **(a)** The intensity (here in terms of the electric field norm squared) along the direction of propagation is show for different angles. **(b)** Comparing the FWHM of the central beam at its maximum as given in the simulations is compared to is FWHM given by $\frac{\Delta r}{2}$.
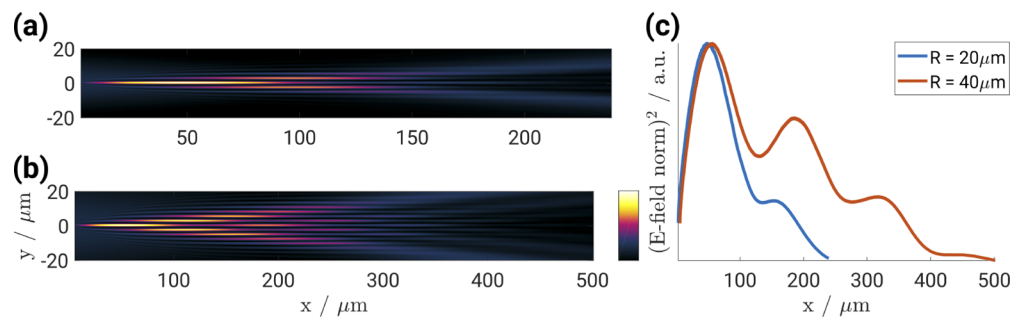
Fig. 6. Simulation results for an axicon with **(a)** $R = 20$ μm and **(b)** $R = 40$ μm at a vacuum wavelength of $\lambda_0 = 532$ nm, $n_i = 2.0559$, $n_o = 1.3371$ at an axicon angle of $\alpha = 8°$. Presented is the square of the electric field norm as an indicator of the light intensity. Panel **(c)** shows the intensity profiles along the central part of the output for the two axicon, both normalized to their maximum value. The FWHM at maximum intensity are 1.47 μm and 1.45 μm for the $R = 20$ μm and $R = 40$ μm axicons respectively. The geometrically expected FWHM is 1.31 μm for both cases.

after the axicon. Most of the lobes appear after that point, where the relevant central lobe has lost most of its intensity already as can be seen in Fig. 6(**c**). The further away from the center these side lobes appear, the farther along the direction of propagation and the weaker they appear. In addition to diminishing of the central beam along the the way, especially the wider on-chip axicon produces a beam with an additional intensity modulation. Finally do the simulation results not only show that the actually relevant DOF is much shorter than geometrically expected, it should be pointed out that the out-of-plane divergence, depending on the thickness of the waveguide reduces the light intensity that is reached away from the axicon even further.

2.3.3. On-chip axicon counter-propagation

A combination of SIM and LSFM was introduced as lattice light-sheet microscopy [47]. Here, we demonstrate that two opposing axicons as presented in Fig. 7 can be used to generate a pattern as presented in Fig. 8 thus implementing chip-based 1D-lattice light-sheets. The design is based on a waveguide loop, with two opposing waveguide end-facets, each with on-chip axicon and the sample can be placed inside the well. Again a Si_3N_4 rib waveguide design is considered. The two opposing axicons in Fig. 7 generate two counter-propagating 1D-light-sheets as simulated for the axicon. The resulting intensity distribution will resemble to a 1D-light-sheet with additional intensity modulation along the x-axis. The simulation parameters like vacuum wavelength and refractive index are kept the same as for the axicon simulations. The on-chip axicons will basically create structures as the ones described above with an additional modulation along the direction of propagation. This pattern may then be shifted along the optical axis by introducing a phase shift $\Delta\phi$ in one of the waveguide arms. Depending on the angle under which the waves stemming from opposing sides interfere, the modulation frequency can be calculated as

$$d = \frac{\lambda_0}{2\sin(90 - \theta)\,n_o}.$$

(6)

Cropped data from the center of the simulation results (marked by a white rectangle) were extracted and a sinusoidal function of the form

$$f(x) = a_1 + a_2\cos(2a_3x\pi - a_4)$$

(7)

was fitted against the data. The parameters a_1, a_2, and a_4 represent the offset, modulation and phase respectively. The pattern wavelength is given by $d = \frac{1}{a_3}$, yielding values of $d = 199$ nm, 200 nm and 201 nm for $\alpha = 8°$, 10° and 15° respectively. These values coincide with the values given by Eq. (6). It can be appreciated that waveguide chip illumination can easily generate counter-propagating Bessel beams with an interfering angle of 180 degrees and thus creating fringe period much smaller than what would have been possible using an objective lens. Moreover, as the light pattern is not generated by the imaging objective lens, it allows free choice of imaging objective lens of different magnification and N.A. without influencing the light pattern generated by the chip-illumination.

2.3.4. On-chip double axicon

Next, we investigate the generation of SBB or bottle beams, using a photonic-chip. It has been previously shown that the interference of two Bessel beams with different radial propagation constants generates an interference pattern described by Eq. (3). This interference pattern is called SBB or bottle beam since it shows zero intensity spots on the optical axis that are surrounded by non-zero light intensity. It is possible to generate such overlapping Bessel beams using an axicon with two different angles. Here the implementation of a chip based double axicon (Fig. 3) is simulated. Simulation results for the chip-based double axicon are presented in Fig. 9. On the left-hand side a COMSOL model with a geometry as presented in Fig. 3 and $n_i = 2.0559$,
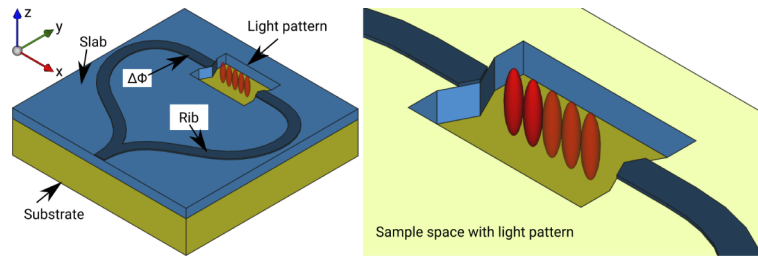
Fig. 7. A photonic chip incorporating two axicons that generate two counter-propagating QBBs with an intensity modulation suitable for SIM. Introducing a phase shift ΔΦ in one arm will shift the generated interference pattern along the *x*-axis. Depending on the axicon width a waveguide taper as shown in Fig. 1 may be required. Phase control is achieved by thermo-optic means as indicated in Fig. 1.
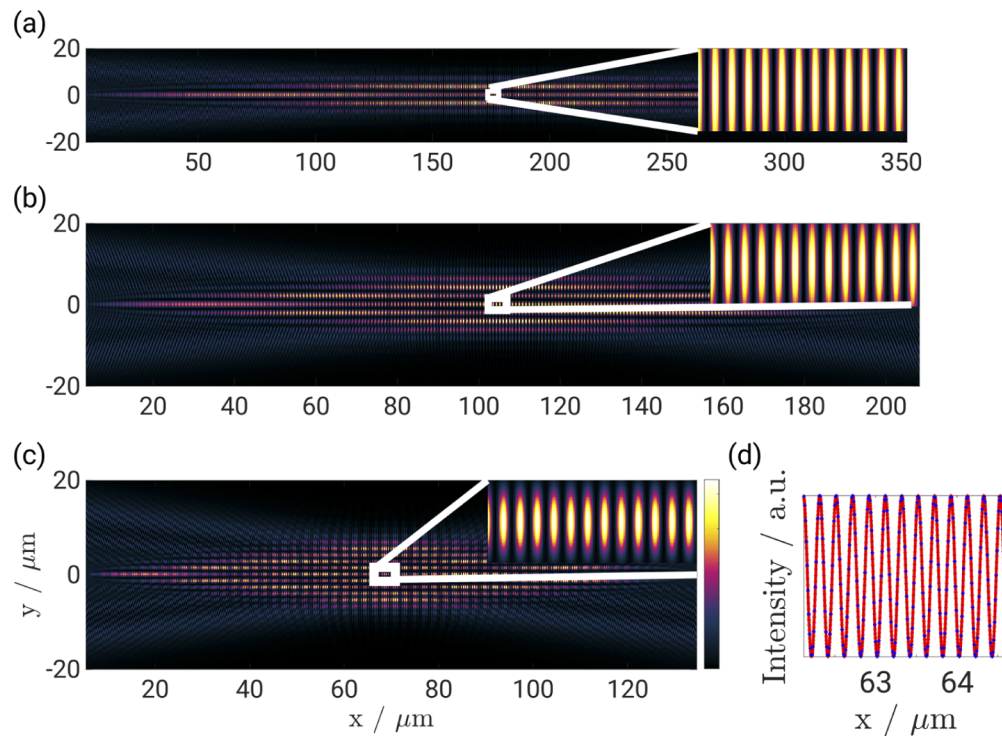

Fig. 8. Using a configuration as presented in Fig. 7, the simulated intensity distribution is shown for axicon angles (as defined in Fig. 2(**c**)) of $\alpha = 6°$, $10°$ and $15°$ as presented in (**a**) – (**c**) respectively. Data samples are taken from the highlighted rectangular regions and a sinusoidal function (see Eq. (7)) is fitted (red curve) to the data (blue dots) to extract the pattern period; an example is shown in (**d**) for the pattern in (**c**). The pattern periods are found to be 199 nm, 200 nm and 201 nm.

$n_o = 1.3371$, $\alpha_1 = 12°$, $\alpha_2 = 3°$ and $6°$, $R_1 = 20\,\mu m$, $R_2 = R_1 \frac{\alpha_2}{\alpha_1}$ is simulated. The fundamental mode propagating in the waveguide is simulated and the intensity distribution after x_2^{min} is presented. On the right-hand side the intensity distribution of two co-propagating Bessel beams as described in Eq. (3) is shown. As opposed to what was done in [40,43], here $\alpha_1 > \alpha_2$. The reason for that is that the geometrical optics approach to the problem suggests that as shown in Fig. 3(b) the light stemming from the first axicon angle and the light stemming from the second axicon angle would not overlap which is actually generating the interference.
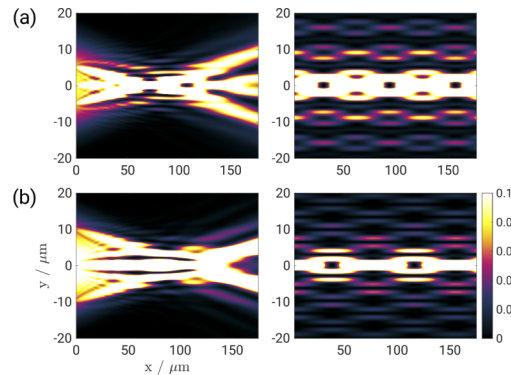

Fig. 9. The output of the on-chip double axicon as simulated in COMSOL on the left-hand side and the corresponding result as per Eq. (3) on the right-hand side. Displayed is the normalized intensity, cut off at 10 % to achieve a representation similar to what is shown in [40,43]. The axicon angles are set to be $\alpha_1 = 12°$ and $\alpha_2 = 3°$ and $6°$ for **(a)** and **(b)** respectively. The axicon size is set to $R_1 = 20\,\mu m$ and $R_2 = R_1 \frac{\alpha_2}{\alpha_1}$ to obtain a good overlap of the green and red region in Fig. 3(b).

As can be seen from the results, a clear intensity void is only expected for $\alpha_2 = 3°$, as shown in Fig. 9(a). The deviation from the result on the right-hand side is basically due to the far from optimal approximation of the two Bessel beams with respect to the spatial extend. This further suggests that it is beneficial to perform simulations based on finite element method for optimizing the design parameters of on-chip lens for free-space beam shaping.

3. Design and simulation of chip-based dynamic beam shaping in free space

In the preceding section, using an on-chip axicon lens approach, the generation of spatially confined, but static illumination patterns is investigated. Moreover, non-flat ends of the end facet of the waveguides are required for the on-chip axicon. Another possibility of on-chip wavefront shaping to generate user-defined illumination patterns is the OPA as illustrated in Fig. 10. According to the Huygens principle each point of a wavefront may be regarded as the source of a spherical wave. The antennas of an OPA mimic a set of point sources. By manipulating their phase and amplitude relation an overall wavefront can be shaped that is desired to generate a QBB for example [26].

Active beam steering in the far-field using OPAs has been demonstrated in SOI designs using the thermo-optic effect to steer a beam across the array, where the outcoupling was facilitated by grating couplers, enabling steering along the array by using different wavelength of 1500 nm, 1550 nm and 1600 nm [22]. Exploring the capability of OPAs, FDTD simulations of OPAs to shape the wavefront as generated by an axicon have been introduced with an emphasize on the Huygens principle for a vacuum wavelength of 780 nm assuming a cleaved end of the chip instead of grating couplers [26]. A passive far-field-focusing at vacuum wavelength of 1550 nm and 635 nm near the diffraction-limit on a Si_3N_4 platform has been demonstrated [28] as well as
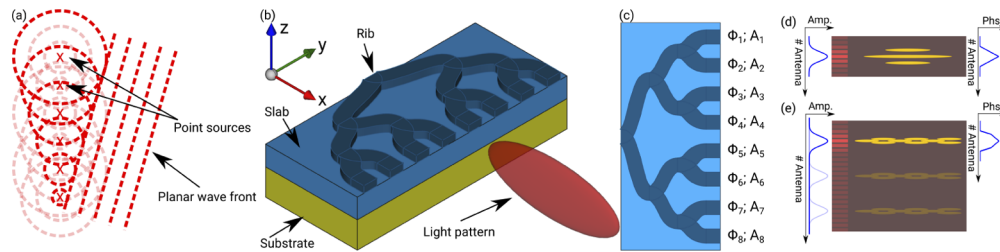
Fig. 10. Beam shaping using an OPA. According to the Huygens principle **(a)** a set of point sources (red x) generates spherical wavefronts (dashed lines) that form a plane wave in the far field. The general concept is presented in **(b)**, the waveguide is presented clinched the *x*-direction. Manipulating the phases ϕ_n and amplitudes A_n in each arm (**(c)**), wavefronts similar to those generated by a (double) axicon are generated in order to obtain QBBs and SBBs. Depending on the amplitude and phase distribution over the antennas, a QBB (**(d)**) or a SBB (**(e)**) may be generated. A dynamic manipulation of ϕ_n and A_n allows for dynamic beam shaping and steering. A spatially extended array may also allow for lateral beam shifting without alteration of the beam profile (**(e)**).

near-field-focusing at a vacuum wavelength of 1550 nm with additional grating based outcoupling and focus steering at a variable vacuum wavelength of 1550 nm, 1560 nm and 1570 nm on a SOI platform [24] which has further been developed to generate a QBB [25].

Regarding the OPA as a set of N antennas located at $\mathbf{r}_n$, radiating isotropically with an amplitude a_n, a phases ϕ_n and a wavelength λ, the complex valued far-field radiation pattern is described by the array factor. Similarly for the near-field a quasi-array-factor model was proposed as [24,25]

$$E(\mathbf{r}) = \sum_{n=1}^{N} = a_n \exp\left[-i\left(2\pi\frac{\|\mathbf{r}_n - \mathbf{r}\|_2}{\lambda}\right) + \phi_n\right]. \tag{8}$$

This way a set of phases ϕ_n can be derived so that N waves constructively interfere at a desired focus spot similar to a plane wave encountering a hyperbolic lens as demonstrated in [24]. In a similar fashion an axially symmetric, linear phase distribution for the generation of a QBB including the required phase distribution have been derived in [25].

3.1. OPA designs at visible wavelengths for one-dimensional QBB

The influence of the amplitude and phase distribution in OPAs is illustrated in Fig. 10. In Fig. 10(**c**) a Gaussian amplitude distribution over a set of waveguides (antennas) is combined with a phase distribution that is symmetrically changing from the center in a linear fashion. The resulting light intensity distribution of a QBB is indicated. In Fig. 10(**e**) the phase distribution has been changed such that it shows two different slopes, thus generating the SBB. Moreover, a lateral movement of the intensity distribution along a larger set of waveguides is indicated by selectively activating different sets of waveguides. In order to test the feasibility of such a design at visible wavelength, not only the quasi-array-factor is calculated but also a two-dimensional FEM model in COMSOL.

Here a Ta_2O_5 on SiO_2 rib waveguide in an aqueous environment at a vacuum wavelength of 660 nm is considered. Assuming a waveguide array consisting of a set of rib waveguides, cleaved at the end of a chip, it is desirable to have good control over the guided modes, preferably single mode conditions in order to apply phase and amplitude control in an orderly fashion. The rib structure for the proposed design is shown in Fig. 11(**a**) and the distribution of the electric field norm of the only guided TE mode is shown in Fig. 11(**b**). The proposed structure shows single mode conditions for the fundamental TE-mode at the given wavelength. In order to perform the

two-dimensional FEM simulations in COMSOL the refractive index for the rib and the slab (n_{rib} and n_{slab} in Fig. 11(a)) are approximated using the dispersion equation as described in [48]. The two-dimensional model in COMSOL is thus set up using two regions with n_{rib} and n_{slab} for the array and one region with the refractive index of water in which the light is propagating. For the quasi-array-factor model only the refractive index of water is considered since a discrete set of point sources is set up.
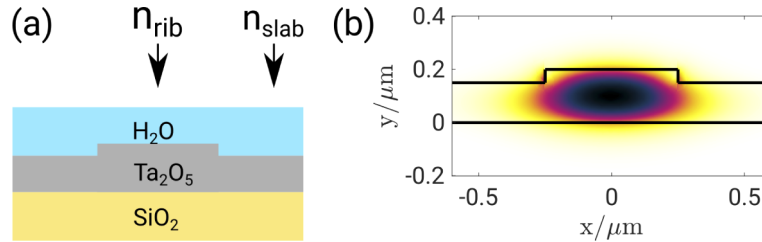

Fig. 11. The waveguide structure in the phased arrays. **(a)** The Ta_2O_5 on SiO_2 structure covert with water is shown. The slab height is 200 nm, the rib height and width are 50 nm and 500 nm respectively. Using a vacuum wavelength of 660 nm only the fundamental TE mode is guided. The distribution of the electric field norm is presented in **(b)** in arbitrary units.

In order to generate a QBB using an OPA, simulations have been performed as presented in Fig. 12. For an array with 16 antennas, a Gaussian amplitude distribution (Fig. 12(c)), and a linear phase distribution (Fig. 12(d)) the generated intensity distribution is simulated. Similar to what has been done for the $N = 64$ array with a spacing (pitch) of $d = 10\,\mu m$ and a propagation wavelength of 1550 nm [25], here the set of $N = 16$ antennas is positioned with $d = 1.5\,\mu m$ and a wavelength of $\lambda = \lambda_0/n_{H_2O}$ for the calculation of the array factor. The square of the electric field norm as obtained from the array factor Eq. (8) is presented in Fig. 11(a) and the equivalent result of the COMSOL simulation is presented in Fig. 12(b). Both results show a similar quality of the generated QBB although the array factor in addition shows tilted versions of the QBB that are less prominent in the FEM simulation that uses actual waveguides of 500 nm width to simulate the array.
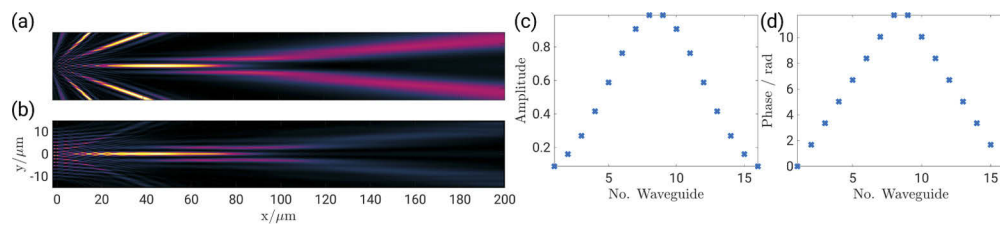

Fig. 12. Given an OPA with 16 elements, the output has been simulated using **(a)** Eq. (8) and **(b)** FEM in COMSOL. The applied amplitude and phase distribution among the waveguides is shown in **(c)** and **(d)** respectively.

In order to generate a SBB as it is described for the double axicon, the $N = 16$ OPA that generates a QBB is extended to $N = 32$ and while maintaining a Gaussian amplitude distribution (Fig. 13(c)), the phase distribution introduces a second slope angle in order to generate two overlapping QBB. Again the array factor and a COMSOL-model are used to simulate the intensity distribution in terms of the square of the electric field norm in Fig. 13(a) and Fig. 13(b) respectively. As for the QBB the array factor simulation of the SBB shows tilted copies of the

intended intensity distribution. This is a feature of the point source model under consideration and the FEM models show a more accurate result since they consider actual waveguide structures.
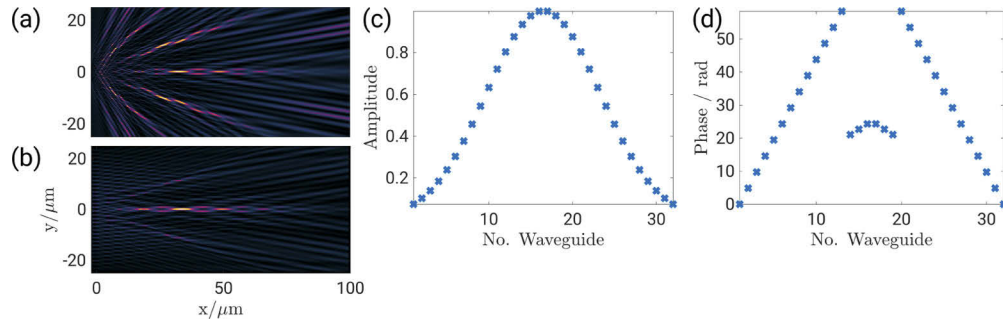

Fig. 13. Given an OPA with 32 elements, the output has been simulated using **(a)** Eq. (8) and **(b)** FEM in COMSOL. The applied amplitude and phase distribution among the waveguides is shown in **(c)** and **(d)** respectively.

The individual manipulation of the OPA's phases allows for a steering of the QBB and SBB. This is demonstrated in Fig. 14**(a)** where a linear phase gradient is added to the original distribution that is used to generate the SBB (Fig. 14**(b)**). This effect has been described with respect to a OPA's ability to shift a focus normal to the optical axis [24], where a linear phase gradient was added as well and the authors find that this approach would not only shift the focus, but will also change the focal length, which has to be corrected for. Looking at the SBB the interpretation is that the beam is not shifted, but tilted and the focal length would actually be the same. An animation of the incremental change for a $-\pi/2$ to a $\pi/2$ distribution is presented in Visualization 1.
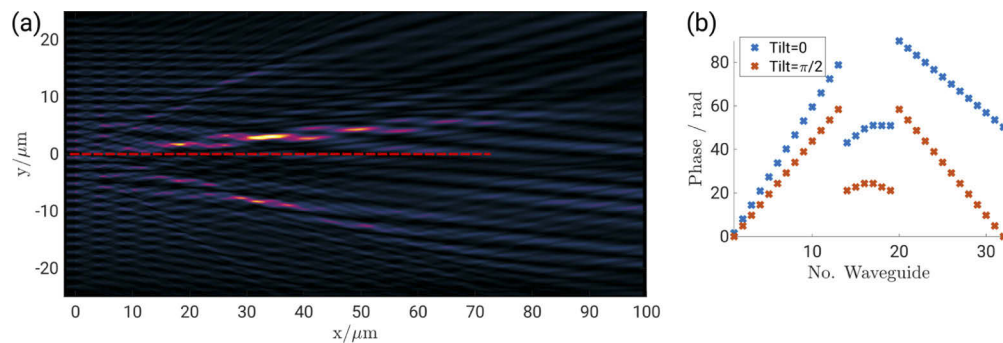

Fig. 14. A similar setup as shown in Fig. 13 is used to demonstrate the tilting capabilities of the OPA. A linear phase gradient of $n\pi/2$ with the waveguide number n is added to the original (red) phase distribution thus changing it to the blue distribution in **(b)**. The SBB in **(a)** is thus tilted from its original optical axis (dashed red line) to an angled direction. See also Visualization 1.

On the other hand it is also possible to change the "focal length" of the SBB and thus move the intensity minima along the optical axis. This is achieved by changing the slope of the linear phase gradient introduced in the OPA. Given a slope for the linear phase gradient for the inner part of the double axicon (symmetric to both sides), a constant offset is is used to generate the slope for the outer part of the double axicon (again in a symmetric manner). Then changing the initial slope for the phase gradient will ultimately shift the SBB along the optical axis. The intensity distribution shown in Fig. 15**(a)** is generated using a phase gradient changing by 8π

from one antenna to the next for the outer and 24π for the inner part. In Fig. 15(**b**) the intensity distribution generated a phase gradient step of $\pi/2$ on the outer part and 16.5π on the inner part is shown. Four minima are indicated in the figures and their shift along the optical axis is the result of a general stretch of the pattern. The phase distributions of Fig. 15(**a**) and Fig. 15(**b**) are shown in Fig. 15(**c**) in blue and red respectively. An incremental shift of the SBB along the optical axis is shown in Visualization 2.
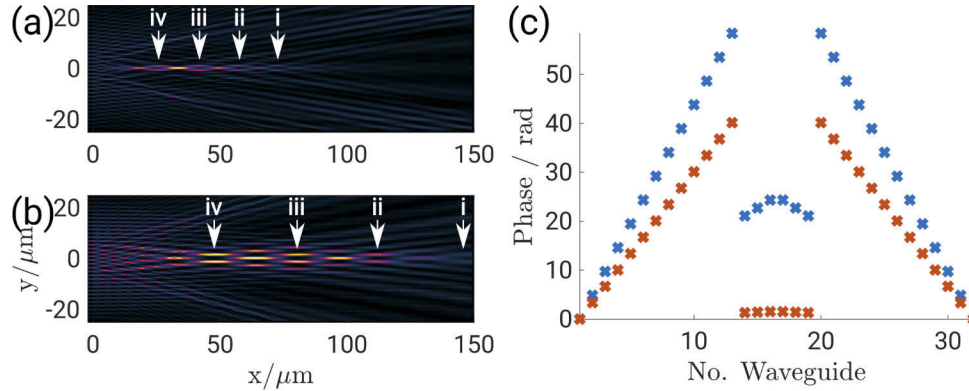

Fig. 15. Manipulating the phase distribution of the OPA in order to shift the intensity minima (i, ii, iii, iv) of the SBB along the optical axis. The intensity distributions presented in (**a**) and (**b**) are generated with the phase distributions presented in (**c**) in blue and red respectively. See also Visualization 2.

4. Fabrication constraints

The fabrication of an actual axicon does involve a deviation from the perfectly sharp tip of the axicon as modeled in this work towards a rounded shape depending on the fabrication tolerance. These deviations have been modeled and investigated as tips of hyperbolic shape [49], as well as spherically shaped tips [50]. With respect to the generated QBBs a modulation of the intensity along the optical axis, as well as a broadening of the central lobe near the axicon were reported.

In [49] the sharp axicon tip is approximated by a hyperbolic shape of the form

$$x = \sqrt{a^2 + \frac{y^2}{\tan^2(\tau/2)}}, \qquad (9)$$

with the parameter a determining the deviation from the perfect shape, the radial coordinate y and the axicon angle $\tau = 180° - 2\alpha$. In order to check the severity of this effect, an axicon as presented in Figs. 4 and 5 (with $\alpha = 6°$) was remodeled with a tip shaped using the hyperbolic approximation with $a = 1$ μm. With the intended micro fabrication process in mind this is a reasonable assumption. This yields a deviation of the tip shape as shown in Fig. 16(**a**). The intensity profiles along the optical axis are plotted in Fig. 16(**b**).

The exemplary simulation of a tip showing hyperbolic shape does show a shift of the intensity distribution along the optical axis. However, a modulation as presented in [49] could not be reproduced. The reason for this may be the use of guided modes instead of freely propagating Gaussian modes as used in [49] and the overall dimensions of the targeted axicons. The broadening of the central lobe as demonstrated in [50] due to a spherical shape of the tip was demonstrated to happen mainly near the axicon such that a significant part of the QBB will be available for the intended application.
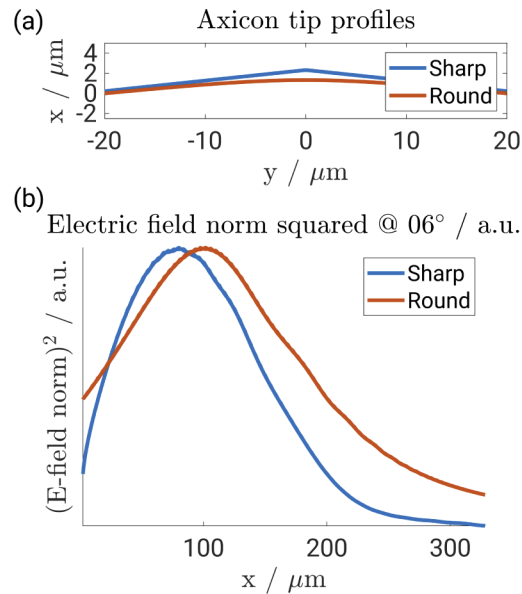
Fig. 16. The profile of the axicon tip is expected to deviate from a perfectly sharp to a round shape due to fabrication limitations. In **(a)** the perfectly sharp and a rounded (hyperbolic) tip profile are shown. The resulting intensity profile of the qbbs are shown in **(b)**.

However, should the fabrication of the on-chip axicon turn out to deviate from the perfectly shaped axicon in such a way, that the generated beam structure may not be applied in the intended way, the use of OPAs can solve this problem. These devices are investigated in section 3 with their ability to generate QBBs among others. The fabrication of flat end faces is not as critical as the fabrication of an axicon and the dynamic phase control allows for adjustment of the intended wavefront.

5. Conclusion

The use of optical waveguides, for performing light beam shaping in free-space optimized for three-dimensional bioimaging applications is investigated. We explore both, the static and the dynamic light shaping using different chip designs, highlighting the suitability and the benefits of integrated photonics in microscopy. This study will lay the foundation for the development of chip-based three-dimensional optical microscopy. The chip-based axicon presents itself as a suitable means to generate light-sheet illumination as used in LSFM, based on a QBB intensity profile. Furthermore the counter propagating configuration of two axicons in combination with thermo-optic phase control has the potential to generate illumination patterns suitable in lattice light-sheet microscopy. The chip enables interference of two counter-propagating Bessel beams with an angle of 180° between them, consequently generating a lattice light-sheet with small interference fringes, which will be beneficial for enhancing the lateral resolution.

Although limited in its extend the simulations of the chip-based double axicon show a general feasibility with respect to SBB generation. The formation of three-dimensional dark spots (bottles) using SBB could find application in chip-based STED. Finally, we explored OPAs in the chip-based implementation, showing to be a useful tool not only in order to generate QBBs and SBB. They are also suitable for dynamic manipulation of the generated beam structure.

It was observed that the FEM simulations in COMSOL provide better overview as opposed to the analytical simulation of the light distribution of the waveguide designs proposed in this work.

This facilitates the actual fabrication of planar waveguides that aid in the shaping of different illumination patterns for different microscopy methodologies. All simulations are performed for visible wavelengths that are essentially used in optical microscopy.

The main motivation of this study is to propose the use of photonic-chips for LSFM and its variants, such as lattice light-sheet microscopy. The main advantage of using photonic-chips is that the entire beam generation and beam steering can be performed using a photonic-chip and thus a standard optical microscope equipped with a single objective lens can be used to acquire LSFM images. This will not only make the setup compact, but also allow easy operation with respect to placement of samples and working distances which are usually restricted with dual-objective lens based LSFM solutions.

Furthermore, the generation of user-defined illumination patterns using a photonic-chips could also have other applications, like optical trapping [51], on-chip Raman spectroscopy [52] and other integrated optical functions.

Funding

References

1. R. Heintzmann and C. G. Cremer, "Laterally modulated excitation microscopy: improvement of resolution by using a diffraction grating," in *Proc. SPIE 3568, Optical Biopsies and Microscopic Techniques III*, I. J. Bigio, H. Schneckenburger, J. Slavik, K. Svanberg, and P. M. Viallet, eds. (International Society for Optics and Photonics, 1999), pp. 185–196.
2. M. G. L. Gustafsson, "Surpassing the lateral resolution limit by a factor of two using structured illumination microscopy," J. Microsc. **198**(2), 82–87 (2000).
3. S. W. Hell and J. Wichmann, "Breaking the diffraction resolution limit by stimulated emission: stimulated-emission-depletion fluorescence microscopy," Opt. Lett. **19**(11), 780–782 (1994).
4. E. Betzig, G. H. Patterson, R. Sougrat, O. W. Lindwasser, S. Olenych, J. S. Bonifacino, M. W. Davidson, J. Lippincott-Schwartz, and H. F. Hess, "Imaging intracellular fluorescent proteins at nanometer resolution," Science **313**(5793), 1642–1645 (2006).
5. S. T. Hess, T. P. Girirajan, and M. D. Mason, "Ultra-high resolution imaging by fluorescence photoactivation localization microscopy," Biophys. J. **91**(11), 4258–4272 (2006).
6. M. J. Rust, M. Bates, and X. Zhuang, "Sub-diffraction-limit imaging by stochastic optical reconstruction microscopy (STORM).," Nat. Methods **3**(10), 793–796 (2006).
7. M. Heilemann, S. Van De Linde, M. Schüttpelz, R. Kasper, B. Seefeldt, A. Mukherjee, P. Tinnefeld, and M. Sauer, "Subdiffraction-resolution fluorescence imaging with conventional fluorescent probes," Angew. Chem., Int. Ed. **47**(33), 6172–6176 (2008).
8. T. Dertinger, R. Colyer, G. Iyer, S. Weiss, and J. Enderlein, "Fast, background-free, 3D super-resolution optical fluctuation imaging (SOFI)," Proc. Natl. Acad. Sci. **106**(52), 22287–22292 (2009).
9. I. Yahiatene, S. Hennig, M. Müller, and T. Huser, "Entropy-Based Super-Resolution Imaging (ESI): From Disorder to Fine Detail," ACS Photonics **2**(8), 1049–1056 (2015).
10. J. Huisken, J. Swoger, F. Del Bene, J. Wittbrodt, and E. H. Stelzer, "Optical sectioning deep inside live embryos by selective plane illumination microscopy," Science **305**(5686), 1007–1009 (2004).
11. A. H. Voie, D. H. Burns, and F. A. Spelman, "Orthogonal-plane fluorescence optical sectioning: three-dimensional imaging of macroscopic biological specimens," J. Microsc. **170**(3), 229–236 (1993).
12. J.-C. Tinguely, Ø. I. Helle, and B. S. Ahluwalia, "Silicon nitride waveguide platform for fluorescence microscopy of living cells," Opt. Express **25**(22), 27678–27690 (2017).
13. B. Agnarsson, A. B. Jonsdottir, N. B. Arnfinnsdottir, and K. Leosson, "On-chip modulation of evanescent illumination and live-cell imaging with polymer waveguides," Opt. Express **19**(23), 22929–22935 (2011).
14. S. Mittler, "Waveguide evanescent field fluorescence and scattering microscopy: The status quo," in *Optics, Photonics and Laser Technology*, Springer Series in Optical Sciences, vol. 218 (Springer, 2018), pp. 1–24.
15. H. M. Grandin, B. Städler, M. Textor, and J. Vörös, "Waveguide excitation fluorescence microscopy: A new tool for sensing and imaging the biointerface," Biosens. Bioelectron. **21**(8), 1476–1482 (2006).
16. A. Hassanzadeh, M. Nitsche, S. Mittler, S. Armstrong, J. Dixon, and U. Langbein, "Waveguide evanescent field fluorescence microscopy: Thin film fluorescence intensities and its application in cell biology," Appl. Phys. Lett. **92**(23), 233503 (2008).
17. R. Diekmann, Ø. I. Helle, C. I. Øie, P. McCourt, T. R. Huser, M. Schüttpelz, and B. S. Ahluwalia, "Chip-based wide field-of-view nanoscopy," Nat. Photonics **11**(5), 322–328 (2017).

18. Ø. I. Helle, D. A. Coucheron, J.-C. Tinguely, C. I. Øie, and B. S. Ahluwalia, "Nanoscopy on-a-chip: super-resolution imaging on the millimeter scale," Opt. Express **27**(5), 6700–6710 (2019).

19. Ø. I. Helle, F. T. Dullo, M. Lahrberg, J.-C. Tinguely, and B. S. Ahluwalia, "Structured illumination microscopy using a photonic chip," arXiv preprint arXiv:1903.05512 (2019).

20. O. G. Hellesø, P. Løvhaugen, A. Z. Subramanian, J. S. Wilkinson, and B. S. Ahluwalia, "Surface transport and stable trapping of particles and cells by an optical waveguide loop," Lab Chip **12**(18), 3436–3440 (2012).

21. B. S. Ahluwalia and O. G. Hellesø, "Optical waveguide loop for planar trapping of blood cells and microspheres," in *Optical Trapping and Optical Micromanipulation X*, vol. 8810 (2013), p. 88100T.

22. K. Van Acoleyen, W. Bogaerts, J. Jágerská, N. Le Thomas, R. Houdré, and R. Baets, "Off-chip beam steering with a one-dimensional optical phased array on silicon-on-insulator," Opt. Lett. **34**(9), 1477–1479 (2009).

23. C. V. Poulton, A. Yaacobi, D. B. Cole, M. J. Byrd, M. Raval, D. Vermeulen, and M. R. Watts, "Coherent solid-state LIDAR with silicon photonic optical phased arrays," Opt. Lett. **42**(20), 4091–4094 (2017).

24. J. Notaros, C. V. Poulton, M. Raval, and M. R. Watts, "Near-Field-Focusing Integrated Optical Phased Arrays," J. Lightwave Technol. **36**(24), 5912–5920 (2018).

25. J. Notaros, C. V. Poulton, M. J. Byrd, M. Raval, and M. R. Watts, "Integrated optical phased arrays for quasi-Bessel-beam generation," Opt. Lett. **42**(17), 3510–3513 (2017).

26. A. Diaz Tormo and N. Le Thomas, "On-chip axicon for light sheet microscopy," in *Proceedings of the 20th Annual Symposium of the IEEE Photonics Society Benelux Chapter*, (2015), pp. 1–4.

27. D. N. Hutchison, J. Sun, J. K. Doylend, R. Kumar, J. Heck, W. Kim, C. T. Phare, A. Feshali, and H. Rong, "High-resolution aliasing-free optical beam steering," Optica **3**(8), 887–890 (2016).

28. C. V. Poulton, M. J. Byrd, M. Raval, Z. Su, N. Li, E. Timurdogan, D. Coolbaugh, D. Vermeulen, and M. R. Watts, "Large-scale silicon nitride nanophotonic phased arrays at infrared and visible wavelengths," Opt. Lett. **42**(1), 21–24 (2017).

29. J. W. Goodman, "Introduction to Fourier Optics, Third Edition", (2004).

30. J. Durnin, "Exact solutions for nondiffracting beams I The scalar theory," J. Opt. Soc. Am. A **4**(4), 651–654 (1987).

31. J. Durnin, J. Miceli, and J. H. Eberly, "Diffraction-free beams," Phys. Rev. Lett. **58**(15), 1499–1501 (1987).

32. Z. Bouchal, J. Wagner, and M. Chlup, "Self-reconstruction of a distorted nondiffracting beam," Opt. Commun. **151**(4-6), 207–211 (1998).

33. S. Chávez-Cerda, E. Tepichin, M. A. Meneses-Nava, G. Ramirez, and J. M. Hickmann, "Experimental observation of interfering Bessel beams," Opt. Express **3**(13), 524–529 (1998).

34. J. H. McLeod, "The Axicon: A New Type of Optical Element," J. Opt. Soc. Am. **44**(8), 592–597 (1954).

35. A. C. S. van Heel, "High Precision Measurements with Simple Equipment*," J. Opt. Soc. Am. **40**(12), 809–816 (1950).

36. Z. Jaroszewicz, A. Burvall, and A. T. Friberg, "Axicon - the Most Important Optical Element," Opt. Photonics News **16**(4), 34–39 (2005).

37. R. M. Herman and T. A. Wiggins, "Production and uses of diffractionless beams," J. Opt. Soc. Am. A **8**(6), 932–942 (1991).

38. J. Arlt and K. Dholakia, "Generation of high-order Bessel beams by use of an axicon," Opt. Commun. **177**(1-6), 297–301 (2000).

39. D. McGloin, G. C. Spalding, H. Melville, W. Sibbett, and K. Dholakia, "Three-dimensional arrays of optical bottle beams," Opt. Commun. **225**(4-6), 215–222 (2003).

40. B. S. Ahluwalia, X. C. Yuan, and S. H. Tao, "Generation of self-imaged optical bottle beams," Opt. Commun. **238**(1-3), 177–184 (2004).

41. B. S. Ahluwalia, X.-C. Yuan, and S. H. Tao, "Transfer of 'pure' on-axis spin angular momentum to the absorptive particle using self-imaged bottle beam optical tweezers system," Opt. Express **12**(21), 5172–5177 (2004).

42. B. S. Ahluwalia, W. C. Cheong, X.-C. Yuan, L.-S. Zhang, S.-H. Tao, J. Bu, and H. Wang, "Design and fabrication of a double-axicon for generation of tailorable self-imaged three-dimensional intensity voids," Opt. Lett. **31**(7), 987–989 (2006).

43. B. S. Ahluwalia, X. C. Yuan, S. H. Tao, W. C. Cheong, L. S. Zhang, and H. Wang, "Micromanipulation of high and low indices microparticles using a microfabricated double axicon," J. Appl. Phys. **99**(11), 113104 (2006).

44. X. C. Yuan, B. S. Ahluwalia, W. C. Cheong, J. Bu, H. B. Niu, and X. Peng, "Direct electron beam writing of kinoform micro-axicon for generation of propagation-invariant beams with long non-diffracting distance," J. Opt. A: Pure Appl. Opt. **9**(4), 329–334 (2007).

45. L. Li, W. M. Lee, X. Xie, W. Krolikowski, A. V. Rode, and J. Zhou, "Shaping self-imaging bottle beams with modified quasi-Bessel beams," Opt. Lett. **39**(8), 2278–2281 (2014).

46. R. A. A. G. Jonathan and P. Manigo, "Self-imaging, self-healing beams generated by photorefractive volume holography," Opt. Eng. **54**(10), 104113 (2015).

47. B. C. Chen, W. R. Legant, K. Wang, L. Shao, D. E. Milkie, M. W. Davidson, C. Janetopoulos, X. S. Wu, J. A. Hammer, Z. Liu, B. P. English, Y. Mimori-Kiyosue, D. P. Romero, A. T. Ritter, J. Lippincott-Schwartz, L. Fritz-Laylin, R. D. Mullins, D. M. Mitchell, J. N. Bembenek, A. C. Reymann, R. Böhme, S. W. Grill, J. T. Wang, G. Seydoux, U. S. Tulu, D. P. Kiehart, and E. Betzig, "Lattice light-sheet microscopy: Imaging molecules to embryos at high spatiotemporal resolution," Science **346**(6208), 1257998 (2014).

48. K. Okamoto, *Fundamentals of Optical Waveguides* (2006).

49. O. Brzobohatý, T. Cižmár, and P. Zemánek, "High quality quasi-Bessel beam generated by round-tip axicon," Opt. Express **16**(17), 12688–12700 (2008).

50. G. S. Sokolovskii, V. V. Dyudelev, S. N. Losev, M. Butkus, K. K. Soboleva, A. I. Sobolev, A. G. Deryagin, V. I. Kuchinskii, V. Sibbet, and E. U. Rafailov, "Influence of the axicon characteristics and beam propagation parameter M2 on the formation of Bessel beams from semiconductor lasers," Quantum Electron. **43**(5), 423–427 (2013).

51. B. S. Ahluwalia, P. Løvhaugen, and O. G. Hellesø, "Waveguide trapping of hollow glass spheres.," Opt. Lett. **36**(17), 3347–3349 (2011).

52. P. Løvhaugen, B. S. Ahluwalia, T. R. Huser, and O. G. Hellesø, "Serial Raman spectroscopy of particles trapped on a waveguide," Opt. Express **21**(3), 2964–2970 (2013).